Dirac spectrum in piecewise constant one-dimensional (1D) potentials

New Journal of Physics
The open-access journal for physics

Dirac spectrum in piecewise constant one-dimensional (1D) potentials

D P Arovas[1,6], L Brey[2], H A Fertig[3], Eun-Ah Kim[4] and K Ziegler[5]

[1] Department of Physics, University of California, San Diego, CA 92093, USA
[2] Instituto de Ciencia de Materiales de Madrid (CSIC), Cantoblanco 28049, Spain
[3] Department of Physics, Indiana University, Bloomington, IN 47405, USA
[4] Department of Physics, Cornell University, Ithaca, NY 14853, USA
[5] Institut für Physik, Universität Augsburg, D-86135 Augsburg, Germany
E-mail: darovas@ucsd.edu

New Journal of Physics **12** (2010) 123020 (19pp)
Received 5 March 2010
Published 13 December 2010
Online at http://www.njp.org/
doi:10.1088/1367-2630/12/12/123020

Abstract. We study the electronic states of graphene in piecewise constant potentials using the continuum Dirac equation appropriate at low energies and a transfer matrix method. For superlattice potentials, we identify patterns of induced Dirac points that are present throughout the band structure and verify for the special case of a particle–hole symmetric potential their presence at zero energy. We also consider the cases of a single trench and a p–n junction embedded in neutral graphene, which are shown to support confined states. An analysis of conductance across these structures demonstrates that these confined states create quantum interference effects, which evidence their presence.

[6] Author to whom any correspondence should be addressed.

Contents

1. Introduction

Graphene, a single layer of carbon atoms laid out in a honeycomb lattice, is one of the most interesting electronic systems to become available over the last few years [1, 2]. It differs from conventional two-dimensional electron gas (2DEG) systems in that the low-energy physics is governed by a Dirac Hamiltonian rather than the more common form for semiconductors, characterized by an effective mass and a band gap. Because of graphene's unusual properties, the possibility of exploiting it for nanoscale applications has become an area of intense investigation.

Nanophysics in graphene may be investigated in systems with very small physical size scales, such as quantum dots[7] or quantum rings [3]–[8]. More commonly, manipulation at the nanoscale is accomplished by the application of electric fields via gate geometries, subjecting the system to potentials varying on a very short length scale. Much recent work has focused on nanotubes [9], on p–n junctions [10]–[14] and on p–n–p junctions [15, 16], whose behavior in graphene is distinct from that of conventional 2DEGs because of the absence of a gap in the spectrum. Very recently, studies of graphene in superlattice potentials have demonstrated the possibility of 'band structure engineering' of graphene [17, 18]. In particular, for 1D superlattices [19, 20], effective potentials may be designed by which the number of Dirac points at the Fermi energy can be artificially manipulated [21]–[26].

In this work, we study graphene systems in the presence of 1D potentials that are piecewise constant. Our approach models graphene in terms of the Dirac equation, which is valid for potentials that vary slowly on the lattice scale and for which intervalley scattering may be ignored. The allowed energy states for such systems may be found by a transfer matrix method described below. For a 1D superlattice, such problems are reminiscent of dynamical systems with periodically varying parameters. We find that the resulting band structure generically supports a collection of Dirac points at a variety of energies. Dirac points generally appear at energies satisfying $\varepsilon \equiv Ed/\hbar v_{\mathrm{F}} = n\pi$ (E is electron energy, d superlattice period and v_{F} Fermi velocity) for n an integer, at $k_y = 0$, where k_y is the momentum perpendicular to the superlattice axis. For particle–hole symmetric potentials, several Dirac points may appear at $\varepsilon = 0$ for nonvanishing values of k_y [21]–[27]. Generically, other Dirac points are present for $\varepsilon, k_y \neq 0$.

[7] See, for example, [31] and references therein.

We also study geometries with a single p or n region, or with a p–n junction region, embedded in a neutral graphene background. We refer to these as a single trench geometry and an embedded p–n junction, respectively. The trench geometry supports solutions which are localized perpendicular to the trench, and are extended along them [16, 28], at energies where the electron states are evanescent in the neutral graphene for a given $k_y \neq 0$. These states disperse as a function of k_y such that a finite number of them cross zero energy. The embedded p–n junction supports localized solutions as well, which may be interpreted in terms of a pair of overlaid trench spectra. If the two trenches are particle–hole conjugates, the individual trench spectra cross zero energy at the same value of k_y; however, because of tunneling between the trenches, these become avoided crossings rather than Dirac points. At large k_y, the gaps at the avoided crossings may be quite small.

Finally, we consider transport across these systems within the Landauer formalism, for which the transfer matrix method is easily adapted to yield the conductance of the system. We demonstrate that the conductance has distinctive signatures indicative of the confined states which may be contained at non-vanishing k_y for a given embedded structure.

This paper is organized as follows. In section 2, we express the problem of a Dirac particle in a periodic potential in terms of a path-ordered product, and find the band structure of the simplest case of alternating positive and negative potential regions. Section 3 develops the transfer matrix method for handling more general piecewise constant potentials. In section 4, we apply the method for computing the spectrum of localized solutions in trench and embedded p–n junction geometries. Section 5 applies the results of the transfer matrix calculations to compute the conductance of these systems. Finally, we conclude with a summary in section 6.

2. Periodic potential

In the vicinity of a Dirac point at the wavevector $\boldsymbol{K}$, we write the wavevector $\boldsymbol{k} = \boldsymbol{K} + \Delta\boldsymbol{k}$, and the two-component wavefunction as $\psi \equiv \mathrm{e}^{\mathrm{i}\boldsymbol{K}\cdot\boldsymbol{x}}(u/v)$. Assuming a scalar potential $V(x)$ that is independent of the coordinate y, the wavefunction $\phi = (u/v)$ may be chosen as an eigenstate of the Hamiltonian $\widetilde{H} = \mathrm{e}^{-\mathrm{i}\boldsymbol{K}\cdot\boldsymbol{x}}\, H\, \mathrm{e}^{\mathrm{i}\boldsymbol{K}\cdot\boldsymbol{x}}$,

$$\widetilde{H} = \begin{pmatrix} V(x) & \hbar v_{\mathrm{F}}(-\mathrm{i}\partial_x + \mathrm{i}q) \\ \hbar v_{\mathrm{F}}(-\mathrm{i}\partial_x - \mathrm{i}q) & V(x) \end{pmatrix}, \tag{1}$$

where $q = \Delta k_y$. The eigenvalue equation for ϕ may then be recast in matrix form as $\partial_x \phi = M(x)\,\phi$, where

$$M(x) = \begin{pmatrix} -q & \mathrm{i}\kappa(x) \\ \mathrm{i}\kappa(x) & q \end{pmatrix} \tag{2}$$

and

$$\kappa(x) = \frac{E - V(x)}{\hbar v_{\mathrm{F}}}. \tag{3}$$

The solution is

$$\begin{pmatrix} u(x) \\ v(x) \end{pmatrix} = \mathcal{P}\exp\left(\int_0^x \mathrm{d}x' M(x')\right)\begin{pmatrix} u(0) \\ v(0) \end{pmatrix}, \tag{4}$$

where $\mathcal{P}$ denotes the path ordering operator, which places smaller values of x to the right.

We presume $V(x) = V(x+d)$ is periodic, in which case the Bloch condition becomes

$$\begin{pmatrix} u(d) \\ v(d) \end{pmatrix} = \mathrm{e}^{\mathrm{i}\theta_x} \begin{pmatrix} u(0) \\ v(0) \end{pmatrix}, \tag{5}$$

where θ_x is the Bloch phase. This leads to the condition

$$\det[\Lambda - \mathrm{e}^{\mathrm{i}\theta_x}] = 0, \tag{6}$$

where

$$\Lambda = \mathcal{P} \exp\left(\int_0^d \mathrm{d}x M(x) \right). \tag{7}$$

Note that $M^\dagger = -\sigma^x M \sigma^x$, where σ^x is the Pauli matrix, and that $\mathrm{Tr}\, M = 0$. Since $\det(\Lambda) = 1$, the eigenvalues of Λ are given by $\zeta = \frac{1}{2}T \pm \sqrt{T^2 - 4}$, where $T = \mathrm{Tr}\,(\Lambda)$. The energy bands, where the Bloch condition can be satisfied, correspond to the regime $|T| \leqslant 2$. For $|T| > 2$, the wavefunctions grow exponentially and are not normalizable. The mathematical structure here is common to a variety of problems involving linear equations with periodic coefficients [29], such as the classical mechanics setting of a pendulum with periodically varying length.

For a continuous periodic function $V(x)$, the path-ordered exponential is not analytically tractable. However, many of the essential features are reproduced by considering a piecewise constant $V(x)$ of the form

$$V(x) = \begin{cases} lV_1 & \text{if } 0 \leqslant x < d_1, \\ lV_2 & \text{if } d_1 \leqslant x < d_1 + d_2. \end{cases} \tag{8}$$

Piecewise constant potentials in graphene have been studied previously [22, 24, 28] by appealing directly to matching conditions for wavefunctions, which produce results equivalent to those of our formulation. For the present approach, we have $\Lambda = \Lambda_2\, \Lambda_1$, where $\Lambda_j = \exp(M_j d_j)$, where the matrices M_j $(j = 1, 2)$ are as in equation (2), with $\kappa_j \equiv (E - V_j)/\hbar v_\mathrm{F}$ in the off-diagonal elements. The period of $V(x)$ is $d_1 + d_2$. We then have

$$\Lambda_j = \cos\alpha_j \cdot \mathbb{I} + \frac{\sin\alpha_j}{\alpha_j} \cdot M_j d_j, \tag{9}$$

with $\alpha_j = d_j \sqrt{\kappa_j^2 - q^2}$. The resulting trace is

$$T = 2\cos\alpha_1 \cos\alpha_2 + 2\, d_1 d_2\, (q^2 - \kappa_1\kappa_2) \cdot \frac{\sin\alpha_1 \sin\alpha_2}{\alpha_1\, \alpha_2}. \tag{10}$$

This condition is consistent with that for allowed energy states obtained via wavefunction matching [22]. The Bloch condition is satisfied when $|T| \leqslant 2$. It is convenient to define the dimensionless quantities

$$\varepsilon = (E - \langle V \rangle) \cdot \frac{d_1 + d_2}{\hbar v_\mathrm{F}}, \tag{11}$$

$$\omega = \tfrac{1}{2}(V_1 - V_2) \cdot \frac{d_1 + d_2}{\hbar v_\mathrm{F}}, \tag{12}$$

where $\langle V \rangle = (d_1\, V_1 + d_2\, V_2)/(d_1 + d_2)$ is the average potential. We also define the dimensionless wavevector $\theta_y = q\, (d_1 + d_2)$. When V is constant, one finds that $T = 2\cos\sqrt{\varepsilon^2 - \theta_y^2}$, and the Bloch condition is satisfied provided $|E - V| > \hbar v_\mathrm{F} |q|$. This, of course, is the condition that the energy E lies within the Dirac cone.

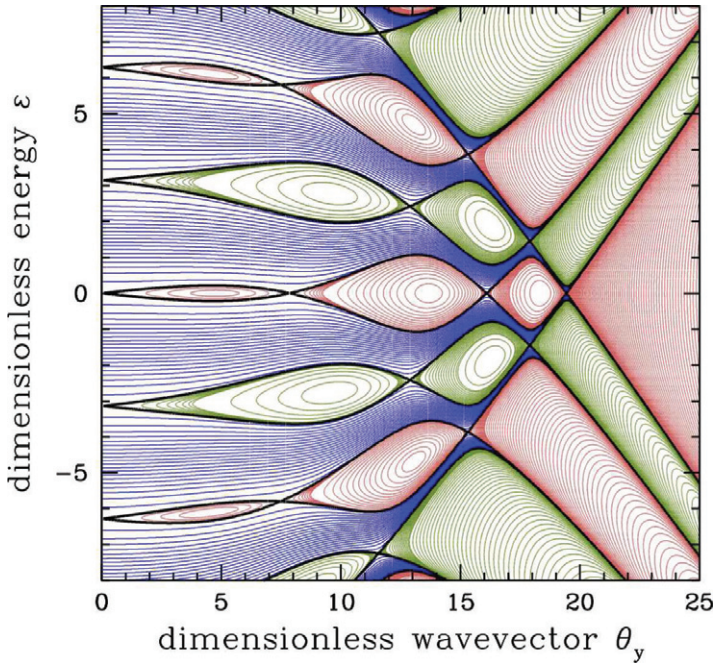

Figure 1. Contour plot of $T = \mathrm{Tr}\,(\Lambda)$ for $d_1 = d_2$ and $\omega = \frac{13}{2}\pi$. Red regions correspond to $T > 2$ and olive regions to $T < -2$. The energy bands are identified by the blue regions, where $|T| < 2$.

Next, consider $V_1 \neq V_2$, but with $q = 0$. The trace is then $T = 2\cos\varepsilon$, and there are allowed states at all energies. The Bloch condition is satisfied marginally when $\varepsilon = n\pi$, corresponding to the touching of two energy bands that disperse with q, to the vanishing of a band gap as $q \to 0$. Indeed, this result holds for arbitrary $V(x)$, since $M(x) = \kappa(x)\,\sigma^x$ in this case; hence $[M(x), M(x')] = 0$ and the path ordering is superfluous.

Now consider the case $d_1 = d_2$. The spectrum then exhibits a particle–hole symmetry relative to $E = \langle V \rangle$. When $E = \langle V \rangle$, $\varepsilon = 0$, we have

$$T = 2 + \left(\frac{2\theta_y \,\sin \frac{1}{2}\sqrt{\omega^2 - \theta_y^2}}{\sqrt{\omega^2 - \theta_y^2}} \right)^2 . \tag{13}$$

Clearly, $T \geqslant 2$, with the marginal condition $T = 2$ pertaining when

$$\theta_y = \pm\sqrt{\omega^2 - 4\pi^2 n^2}\,, \tag{14}$$

where n is an integer, as well as a solution at $\theta_y = 0$. Since q is real, there is a maximum allowed value for n,

$$n_{\max} = \left[\frac{\omega}{2\pi} \right], \tag{15}$$

where the brackets indicate the greatest integer function. Thus, two new Dirac points open up each time ω increases by 2π, and there are $2n_{\max} + 1$ Dirac points, including the one at $\theta_y = 0$. Similar results have previously been obtained by other methods [24]–[26]. (See for example figures 4 and 5 of [24].)

In figures 1 and 2, we plot the contours of the function $T(\varepsilon, \theta_y)$ for $\omega = \frac{13}{2}\pi$ for $d_1 = d_2$ and $d_1 = \frac{2}{3}\,d_2$, respectively. Note the particle hole symmetry present in the former case, which

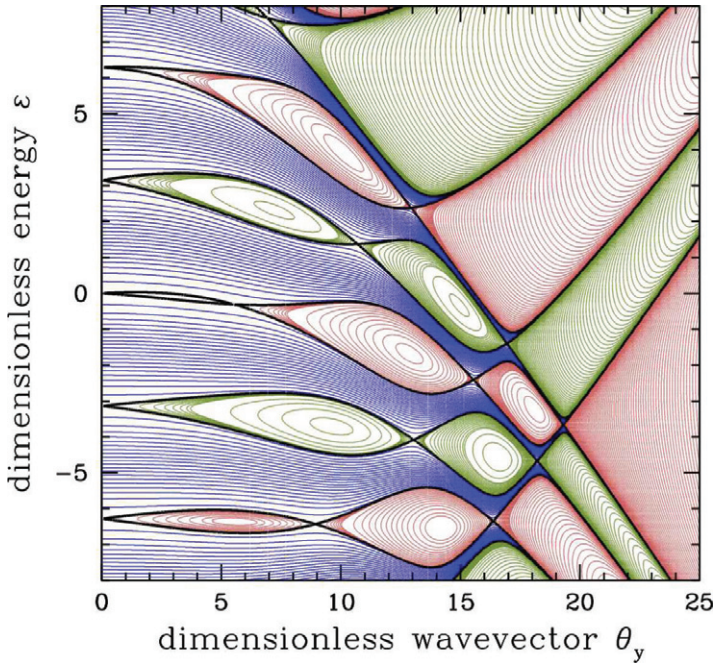

Figure 2. Contour plot of $T = \mathrm{Tr}\,(\Lambda)$ for $\omega = \frac{13}{2}$ and $d_1 = \frac{2}{3}d_2$.

is broken when $d_1 \neq d_2$. Note also the band touchings at $\varepsilon = n\pi$ for $\theta_y = 0$ in both cases. In figure 3, we again plot the band structure as in figure 1, but showing the high-energy structure as well. At energy scales $|\varepsilon| \gg 1$, the spectrum may be understood as the intersection of the two Dirac cones $|\varepsilon + \omega| > \theta_y$ and $|\varepsilon - \omega| > \theta_y$. The presence of a spectrum with such bands and gaps can lead to highly non-trivial behavior in transport through such structures [24].

As a limiting case of the model, consider $d_2 \to 0$ with $V_2 d_2 = -\hbar v_F \Omega_0$ finite. The potential is then

$$V(x) = \Omega_0 \cdot \frac{\hbar v_{\mathrm{F}}}{d} > \left\{1 - \sum_{n=-\infty}^{\infty} \delta\left(\frac{x}{d} - n\right)\right\}, \tag{16}$$

a Dirac comb with a uniform compensating background. The trace in this case is given by

$$T = 2\cos\Omega_0 \cos\alpha - 2\sin\Omega_0 \sin\alpha \cdot \left(\frac{\varepsilon - \Omega_0}{\alpha}\right), \tag{17}$$

where $\alpha = \sqrt{(\varepsilon - \Omega_0)^2 - \theta_y^2}$. This limit is distinguished by the fact that all the Dirac points of $T(\varepsilon, \theta_y)$ lie along the line $\theta_y = 0$, as shown in figure 4.

3. Transfer matrices and Landauer conductance through potential slabs

Consider a piecewise constant potential $V(x)$, as depicted in figure 5, in which $V = V_j$ over a slab of width d_j, with $j = 1, \ldots, N$. We presume the slabs are bounded by pristine regions of graphene with $V = 0$, and we label these outer regions 0 and $N + 1$.

Wavevectors k_j for each of the slabs may be defined by the relations

$$\frac{E}{\hbar v_{\mathrm{F}}} = \sigma_0 k_0 = \frac{V_j}{\hbar v_{\mathrm{F}}} + \sigma_j k_j, \tag{18}$$

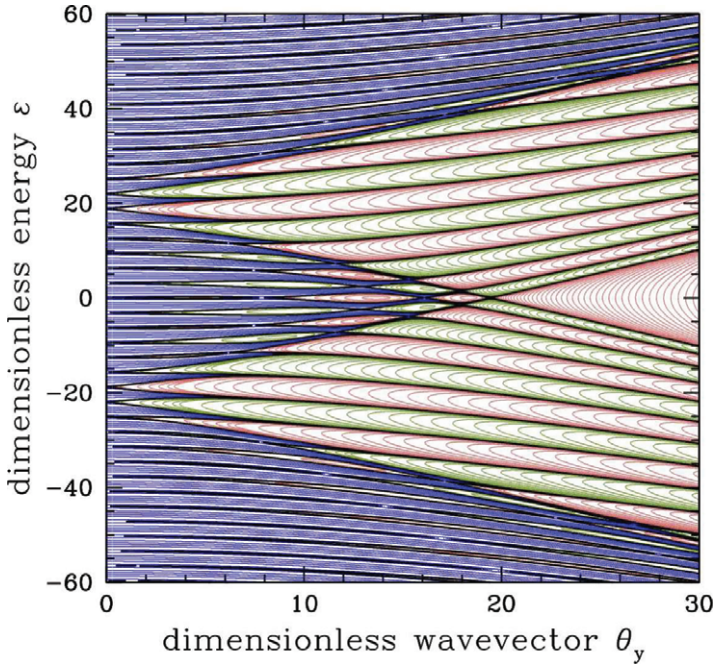

Figure 3. Contour plot of $T = \mathrm{Tr}\,(\Lambda)$ for $\omega_0 = \frac{13}{2}\pi$ and $d_1 = d_2$.

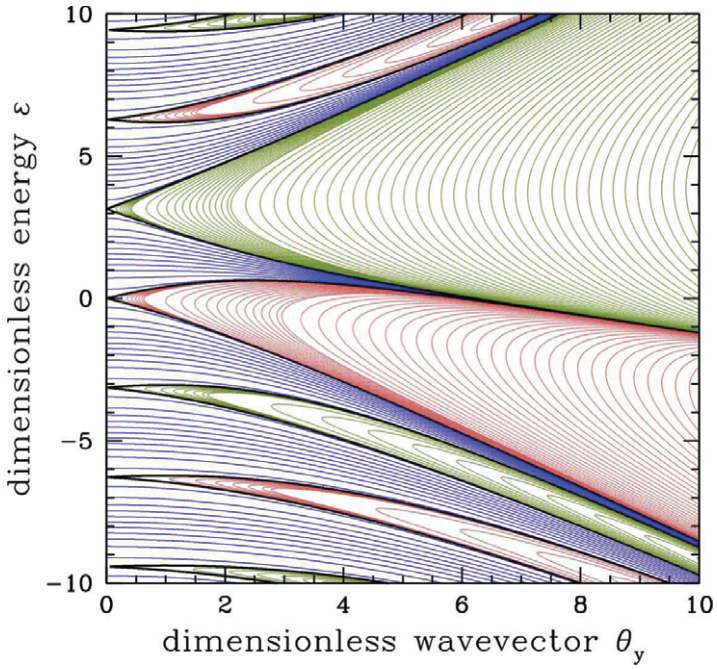

Figure 4. Contour plot of $T = \mathrm{Tr}\,(\Lambda)$ in the $d_2 \to 0$ limit with $\Omega_0 \equiv -V_2 d_2/\hbar v_\mathrm{F} = \frac{3}{5}\pi$ held constant.

where each $k_j \geqslant k0$ is non-negative. Here, $\sigma_j = \pm 1$ is a binary variable in each slab that indicates whether the energy E is above (n-type) or below (p-type) the Dirac point, which occurs at $E = V_j$. We take $\sigma_0 = \sigma_{N+1}$ and $V_0 = V_{N+1} = 0$.

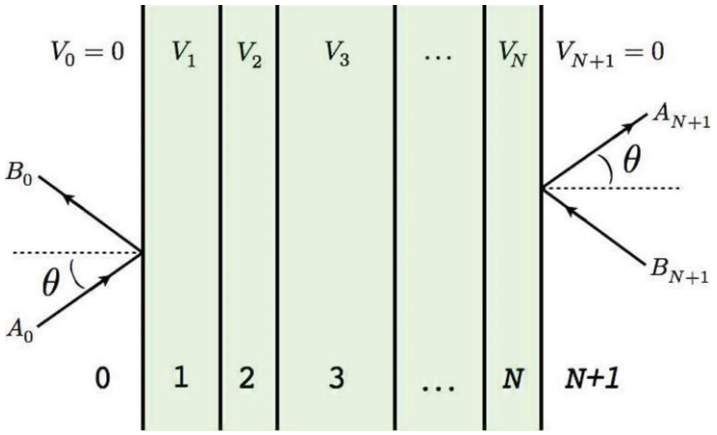

Figure 5. Transport through a series of potential slabs. The potential $V(x)$ is piecewise constant, given by V_j in the jth slab.

In each region j, the solution to the Dirac equation,

$$-\mathrm{i}\hbar v_{\mathrm{F}}\,\boldsymbol{\sigma}\cdot\boldsymbol{\nabla}\psi + V_j\psi = E\psi, \tag{19}$$

is either propagating or evanescent. Due to translation invariance in the y-direction, we are free to fix the wavevector q along this axis; all solutions include a factor $\mathrm{e}^{\mathrm{i}qy}$. The local Fermi wavevector k_j in each region is related to the local density by $n_j = k_j^2/4\pi$, and the sign of the carrier charge is $-\sigma_j$.

If $k_j > q$, the wavefunction in slab j propagates as a plane wave along the x-direction as well. The solution is of the form

$$\psi_j(x) = \left\{ \frac{A_j}{\sqrt{2}} \begin{pmatrix} 1 \\ \sigma_j\,\mathrm{e}^{\mathrm{i}\theta_j} \end{pmatrix} \mathrm{e}^{\mathrm{i}k_j x\cos\theta_j} + \frac{B_j}{\sqrt{2}} \begin{pmatrix} 1 \\ -\sigma_j\,\mathrm{e}^{-\mathrm{i}\theta_j} \end{pmatrix} \mathrm{e}^{-\mathrm{i}k_j x\cos\theta_j} \right\} \mathrm{e}^{\mathrm{i}k_j y\sin\theta_j}, \tag{20}$$

where $\theta \in \left[-\frac{\pi}{2}, \frac{\pi}{2}\right]$. Matching the y dependence gives us the condition

$$q = k_j \sin\theta_j \quad \text{if } k_j \geqslant q. \tag{21}$$

To solve for the wavefunction everywhere, we must match the value of each component of $\psi(x)$ at the boundaries between slabs. Accordingly, from equation (20), we define the matrix

$$M_j = \begin{pmatrix} \frac{1}{\sqrt{2}} & \frac{1}{\sqrt{2}} \\ \frac{1}{\sqrt{2}}\,\sigma_j\,\mathrm{e}^{\mathrm{i}\theta_j} & -\frac{1}{\sqrt{2}}\,\sigma_j\,\mathrm{e}^{-\mathrm{i}\theta_j} \end{pmatrix}, \tag{22}$$

which we shall invoke soon. Free propagation across a slab is described by the transfer matrix

$$K_j = \begin{pmatrix} \mathrm{e}^{\mathrm{i}k_j d_j\cos\theta_j} & 0 \\ 0 & \mathrm{e}^{-\mathrm{i}k_j d_j\cos\theta_j} \end{pmatrix}. \tag{23}$$

If $k_j < q$, the solution in slab j has an evanescent (pure exponential) behavior along the x-axis,

$$\psi_j(x) = \left\{ A_j \begin{pmatrix} \cos\left(\frac{\varphi_j}{2}\right) \\ \mathrm{i}\sigma_j \sin\left(\frac{\varphi_j}{2}\right) \end{pmatrix} \mathrm{e}^{k_j x\cot\varphi_j} + B_j \begin{pmatrix} \sin\left(\frac{\varphi_j}{2}\right) \\ i\sigma_j \cos\left(\frac{\varphi_j}{2}\right) \end{pmatrix} \mathrm{e}^{-k_j x\cot\varphi_j} \right\} \mathrm{e}^{\mathrm{i}k_j y\csc\varphi_j}, \tag{24}$$

where $\varphi_j \in \left[-\frac{\pi}{2}, \frac{\pi}{2}\right]$. Momentum conservation along y requires

$$q = k_j \csc\varphi_j \quad \text{if } k_j \leqslant q. \tag{25}$$

For the evanescent slabs, we define

$$M_j = \begin{pmatrix} \cos\left(\frac{\varphi_j}{2}\right) & \sin\left(\frac{\varphi_j}{2}\right) \\ \\ \mathrm{i}\sigma_j \sin\left(\frac{\varphi_j}{2}\right) & \mathrm{i}\sigma_j \cos\left(\frac{\varphi_j}{2}\right) \end{pmatrix}, \tag{26}$$

and free propagation across an empty slab is described by

$$K_j = \begin{pmatrix} \mathrm{e}^{k_j d_j \cot\varphi_j} & 0 \\ \\ 0 & \mathrm{e}^{-k_j d_j \cot\varphi_j} \end{pmatrix}. \tag{27}$$

The equations guaranteeing continuity of the wavefunction at the slab boundaries are

$$M_{j-1} \begin{pmatrix} A^{\mathrm{R}}_{j-1} \\ \\ B^{\mathrm{R}}_{j-1} \end{pmatrix} = M_j \begin{pmatrix} A^{\mathrm{L}}_{j} \\ \\ B^{\mathrm{L}}_{j} \end{pmatrix}. \tag{28}$$

Here, the superscripts R and L refer to the right and left boundaries of the slab. They are related, within a given slab, by the free propagation transfer matrix,

$$\begin{pmatrix} A^{\mathrm{R}}_{j} \\ \\ B^{\mathrm{R}}_{j} \end{pmatrix} = K_j \begin{pmatrix} A^{\mathrm{L}}_{j} \\ \\ B^{\mathrm{L}}_{j} \end{pmatrix}. \tag{29}$$

We can now compute the transfer matrix $\mathcal{M}$ for a general configuration of slabs, which is defined by the relation

$$\begin{pmatrix} A^{\mathrm{L}}_{N+1} \\ \\ B^{\mathrm{L}}_{N+1} \end{pmatrix} = \mathcal{M} \begin{pmatrix} A^{\mathrm{R}}_{0} \\ \\ B^{\mathrm{R}}_{0} \end{pmatrix}. \tag{30}$$

In terms of the previously defined quantities, the total transfer matrix is

$$\mathcal{M} = M^{-1}_{N+1}(M_N\, K_N\, M^{-1}_N) \cdots (M_1\, K_1\, M^{-1}_1) M_0. \tag{31}$$

The recurring matrices $Q_j = M_j K_j M_j^{-1}$ may be parameterized by θ_j and $\chi_j = kd\cos\theta_j$ for a propagating region and by φ_j and $\omega_j = kd\cot\varphi_j$ for an evanescent region, as detailed in the appendix. As is well known, the transfer matrix relates data on the left to data on the right of a given region. Incoming and outgoing flux amplitudes are related by the S-matrix,

$$\begin{pmatrix} A_{N+1} \\ B_0 \end{pmatrix} = \overbrace{\begin{pmatrix} t & r' \\ r & t' \end{pmatrix}}^{\mathcal{S}} \begin{pmatrix} A_0 \\ B_{N+1} \end{pmatrix}. \tag{32}$$

Appealing to the unitarity of $\mathcal{S}$, we then have

$$\mathcal{M}_{11} = t^{*-1}, \quad \mathcal{M}_{12} = r'\, t'^{-1}, \tag{33}$$

$$\mathcal{M}_{21} = -t'^{-1} r, \quad \mathcal{M}_{22} = t'^{-1}. \tag{34}$$

As discussed in more detail below, the dimensionless two-terminal Landauer conductance, in units of e^2/h per spin channel, is given by

$$T = |t|^2 = |\mathcal{M}_{11}|^{-2}. \tag{35}$$

4. Localized solutions of embedded geometries

We first consider situations where the outer regions contain evanescent waves, so the wavefunction is localized within the slabs. In this case, we must have $B_0 = 0$ and $A_{N+1} = 0$, if $\cot\varphi > 0$, which requires $\mathcal{M}_{11} = 0$; for the case $\cot\varphi < 0$, we must have $A_0 = 0$ and $B_{N+1} = 0$, leading to $\mathcal{M}_{22} = 0$. This condition defines the 1D dispersion $E(q)$, where $q = k_0 \csc\varphi_0 = k_j \sin\theta_j$.

4.1. Single trench

For the single-trench geometry, the existence of localized wavefunctions has been noted previously in [28]. For completeness and later discussion, we explain how they arise in the present formulation. For a single trench of width d, the condition $\mathcal{M}_{11} = 0$ is

$$\cos\varphi_0 \cos\theta_1 \cos\chi_1 + (\sin\theta_1 - \sigma_0\sigma_1 \sin\varphi_0) \sin\chi_1 = 0 \tag{36}$$

or

$$\cos\varphi_0 \cos\varphi_1 \cosh\omega_1 + (1 - \sigma_0\sigma_1 \sin\varphi_0 \sin\varphi_1) \sinh\omega_1 = 0. \tag{37}$$

The condition $\mathcal{M}_{22} = 0$ is obtained by reversing the sign of χ_1 or ω_1. We now define the dimensionless potential $\nu \equiv Vd/\hbar v_F$, energy $\varepsilon \equiv \sigma_0 k_0 d = \nu + \sigma_1 k_1 d$ and wavevector $\theta_y = qd$. The eigenvalue condition is then $F(\varepsilon, \nu, \theta_y) = 0$, where

$$F(\varepsilon, \nu, \theta_y) = (\theta_y^2 - \varepsilon\,(\varepsilon - \nu)) \cdot \frac{\sin\chi_1}{\chi_1} + \sqrt{\theta_y^2 - \varepsilon^2}\cos\chi_1 \tag{38}$$

and

$$\chi_1 = \sqrt{(\varepsilon - \nu)^2 - \theta_y^2}. \tag{39}$$

This form for F holds for either sign of q and is extended to the regime $(\varepsilon - \nu)^2 < \theta_y^2$ via analytic continuation. If we search for eigenvalues at $\varepsilon = 0$, we obtain the condition

$$\frac{\chi_1}{(\nu^2 - \chi_1^2)^{1/2}} = -\tan\chi_1, \tag{40}$$

a graphical analysis of which shows a new root emerging each time ud passes through $n\pi$.[8] Thus, there are $[\nu/\pi]$ solutions with $\varepsilon = 0$ that lie at finite values of θ_y. In figure 6, for example, we have $\nu = 14$ and thus there are $[14/\pi] = 4$ bands that cross $\varepsilon = 0$ at finite θ_y.

4.2. Embedded junction

Consider next the case of an embedded junction with a double step,

$$V(x) = \begin{cases} l0 & \text{if } x < 0, \\ lV_1 & \text{if } 0 \leqslant ax < d_1, \\ lV_2 & \text{if } d_1 \leqslant x < d_1 + d_2, \\ l0 & \text{if } d_1 + d_2 \leqslant x. \end{cases} \tag{41}$$

[8] Note that this equation can be inferred by setting $\varepsilon = 0$ in equation (7) of [28].

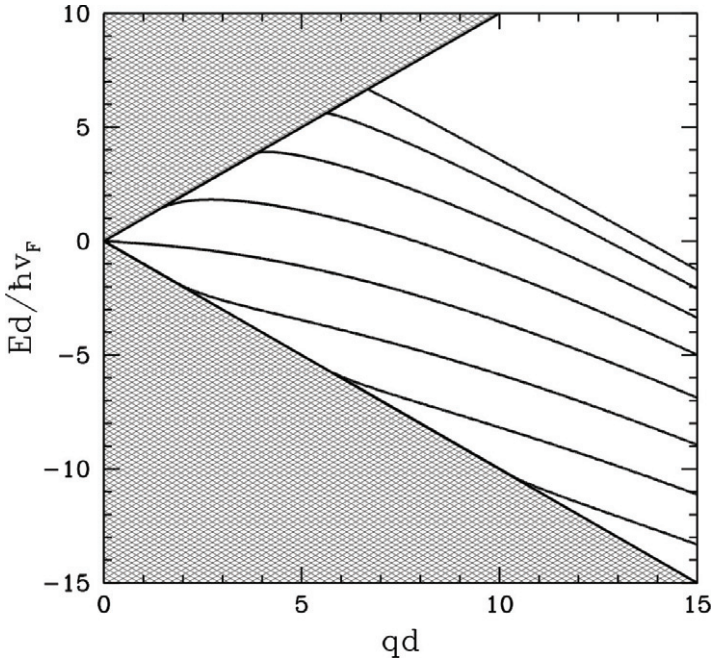

Figure 6. Energy bands for a single trench of width d and potential $V = 14\hbar v_F/d$. The hatched region depicts the Dirac cones in the bulk. Solid lines show dispersions for bands of localized states in the gap between the upper and lower Dirac cones.

When V_1 and V_2 are of opposite sign, this corresponds to a p–n junction embedded in neutral graphene. We define $\varepsilon = \sigma_0 k_0(d_1 + d_2)$, $\theta_y = q(d_1 + d_2)$ and $\nu_j = V_j(d_1 + d_2)/\hbar v_F$. We furthermore define $x_j \equiv d_j/(d_1 + d_2)$, so $x_1 + x_2 = 1$. Applying the transfer matrix formalism, we once again arrive at an eigenvalue condition $F(\varepsilon, \nu_1, \nu_2, x_1, \theta_y) = 0$, this time with

$$F(\varepsilon, \nu_1, \nu_2, x_1, \theta_y) = x_1(\theta_y^2 - \varepsilon\,(\varepsilon - \nu_1)) \cdot \frac{\sin\chi_1}{\chi_1} \cdot \cos\chi_2 + x_2(\theta_y^2 - \varepsilon\,(\varepsilon - \nu_2)) \cdot \cos\chi_1 \cdot \frac{\sin\chi_2}{\chi_2}$$
$$+ \left[x_1 x_2(\theta_y^2 - (\varepsilon - \nu_1)(\varepsilon - \nu_2)) \cdot \frac{\sin\chi_1}{\chi_1} \cdot \frac{\sin\chi_2}{\chi_2} + \cos\chi_1 \cos\chi_2 \right] \cdot \sqrt{\theta_y^2 - \varepsilon^2}, \quad (42)$$

where

$$\chi_j = x_j \sqrt{(\varepsilon - \nu_j)^2 - \theta_y^2}, \quad (43)$$

and where we continue to express energies and wavevectors as dimensionless quantities. As with the single trench case, the expression for F is analytically continued to the regimes where $(\varepsilon - \nu_j)^2 < \theta_y^2$.

Generally speaking, when two semi-infinite undoped regions are separated by a sequence of doped slabs, in addition to the Dirac cones in the bulk, one obtains localized subbands with energies lying within the gap between the upper and lower Dirac cones. The wavefunctions for these subband states are localized within the slabs. In figure 6, we plot the Dirac cones and subband dispersions for the case of a single strip of width d with potential $V = 14\hbar v_F/d$.

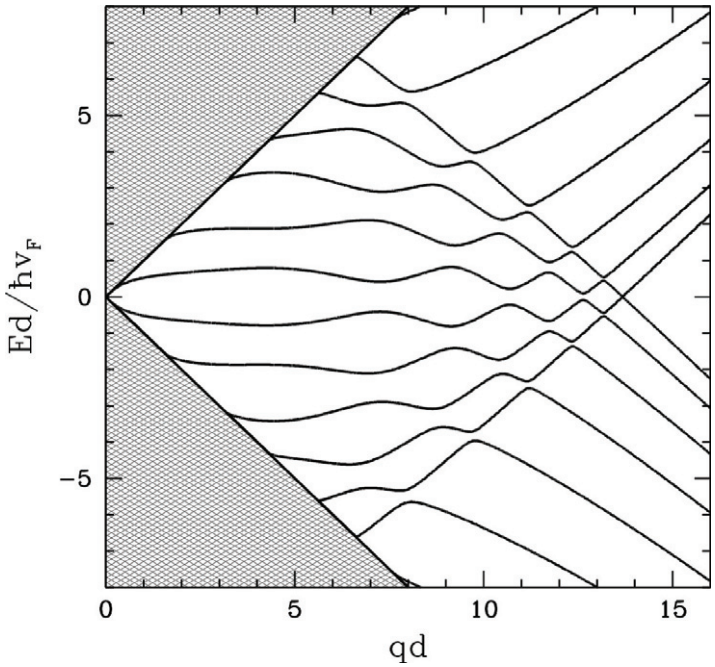

Figure 7. Energy bands for a p–n junction embedded in neutral graphene. Both p and n regions have width d, with $V_1 = -V_2 = 14\hbar v_F/d$. The hatched region depicts the Dirac cones in the bulk. Solid lines show dispersions for bands of localized states in the gap between the upper and lower Dirac cones.

In figures 7 and 8, we investigate the case of a p–n junction embedded in neutral graphene, where both p and n regions have the same width d, and again we choose $V = \pm 14\hbar v_F/d$ for purposes of illustration. Apparently, $E = 0$ always lies within a gap between subbands. Note that the parameters of the p–n junction are such that the spectum is particle–hole symmetric.

The subband structure of a general p–n junction can be understood in terms of the simple diagram in figure 9. In the figure, we sketch the three Dirac cones for the undoped bulk region (black lines), the p-type slab (blue lines, $V_1 d_1/\hbar v_F = 12$) and the n-type slab (red lines, $V_2 d_2/\hbar v_F = -7$). For the purpose of generality, we consider a system that has no particle–hole symmetry. Outside the black hatching, there are no bulk states. In regions I and III, there are localized states living along the p-trench. Similarly, in regions I and II, there are localized states living along the n-trench. In region I, there can be resonant tunneling between the p and n trenches, and the localized states live in both trenches. In region IV, which lies outside all three Dirac cones, there can be no states. In figure 10, we plot the subband structure for this p–n junction, with equal thicknesses of the p and n regions, superimposing on those curves the results for the individual single barrier problems. A comparison with the sketch in figure 9 reveals the basic physics of the energy spectrum. One may see the confined states associated with each of the two trenches, one set dispersing up and the other down. These confined states admix where they are degenerate for the individual trenches, leading to anticrossings. In the case where the two trenches are equal and opposite (e.g. figures 7 and 8), this leads to a set of anticrossings around zero energy, rather than the extra Dirac points one finds in the superlattice case.

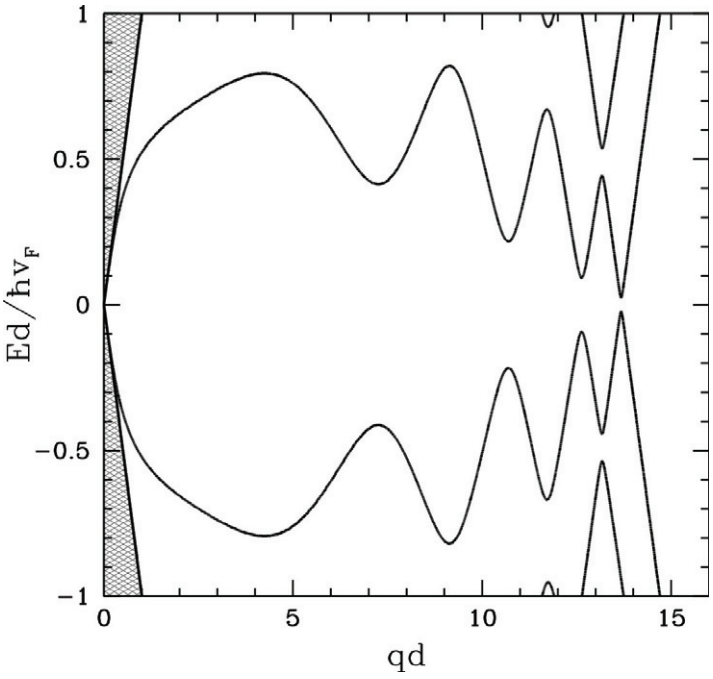

Figure 8. Low-energy detail for the embedded p–n junction from figure 7, showing that $E = 0$ always lies within a gap between subbands.

We conclude this section with a few remarks. Since the presence of localized solutions appears because there is effectively a gap in the spectrum of neutral graphene as a function of k_x when $q \equiv k_y d$ is non-vanishing and fixed, allowing evanescent solutions outside the trench regions, it is clear that localized solutions will be present even if the potential varies smoothly, rather than in the piecewise constant way we have studied. Secondly, it is interesting to note that the very narrow bands at large q for the superlattice spectra (e.g. figures 1 and 2) approximately follow the energies of bound states in the individual trenches making up the superlattice, so that this region of the spectrum may be understood as arising from localized trench states that are weakly coupled together. It is also interesting to note that the avoided crossings of the embedded p–n junction evolve into Dirac points when many of these are joined together to form a superlattice.

5. Two-probe Landauer conductance

In this section, we consider transmission through a slab geometry for the more general case where the graphene leads are doped. Consider the geometry of figure 5. Define a vertical ($\hat{\boldsymbol{y}}$-directed) surface Σ somewhere to the right of the Nth slab. The current across that surface will be the sum of three contributions. Firstly, there will be carriers injected from the left side, with chemical potential μ_{L}, moving at angle $\theta \in \left[-\frac{1}{2}\pi, \frac{1}{2}\pi\right]$, which make it past the slabs with probability $T(E, \theta)$. These are all right-movers. Secondly, there will be carriers from the right lead, with chemical potential μ_{R}, moving at an angle $\theta \in \left[\frac{1}{2}\pi, \frac{3}{2}\pi\right]$. Because of this range of θ, all these are left-movers. Finally, with probability $R'(E, \theta)$, each of these left-moving carriers

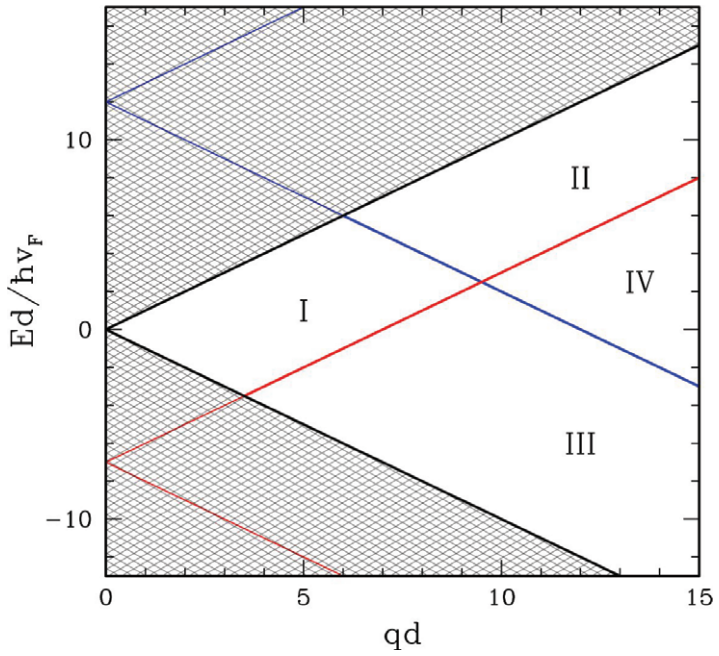

Figure 9. The bulk Dirac cones for $V = 0$ are hatched in black. Localized states in the p trench ($V_1 = 12\hbar v_F/d$) are present in regions I and III. Localized states in the n-trench ($V_2 = -7\hbar v_F/d$) are present in regions I and II.

reflects off the barrier region, scattering into a state with $\theta' = \pi - \theta$. Putting all this together,

$$I_\Sigma = L_\Sigma\, \hat{\boldsymbol{n}}_\Sigma \cdot \int_{-\infty}^{\infty} \mathrm{d}E > \mathcal{N}(E) \int_{-\pi/2}^{\pi/2} \frac{\mathrm{d}\theta}{2\pi} \Big\{ T(E,\theta)\, \boldsymbol{J}(E,\theta)\, f(E-\mu_{\mathrm{L}}) + \Big[\boldsymbol{J}(E,\pi+\theta) + R(E,\pi+\theta)\, \boldsymbol{J}(E,-\theta) \Big] f(E-\mu_{\mathrm{R}}) \Big\}, \tag{44}$$

where L_Σ is the length of the surface and $\mathcal{N}(E)$ is the density of states,

$$\mathcal{N}(E) = \frac{g\,|E|}{2\pi\hbar^2 v_{\mathrm{F}}^2}, \tag{45}$$

and $g = 4$ accounts for spin and valley degeneracy. $\boldsymbol{J}(E,\theta)$ is given by

$$\boldsymbol{J}(E,\theta) = -e v_{\mathrm{F}}\, \mathrm{sgn}(E)\, (\hat{\boldsymbol{x}} \cos\theta + \hat{\boldsymbol{y}} \sin\theta). \tag{46}$$

We take $\hat{\boldsymbol{n}}_\Sigma = \hat{\boldsymbol{x}}$. Unitarity of the S-matrix yields $T(E,\theta) + R(E,\pi+\theta) = 1$. Expanding in the difference $\mu_{\mathrm{L}} - \mu_{\mathrm{R}}$, we obtain at $T = 0$

$$I_\Sigma = \frac{e^2}{\pi h}\, V\, \langle T(E_{\mathrm{F}}) \rangle\, \frac{g\,|E_{\mathrm{F}}|}{\hbar v_{\mathrm{F}}}\, L_y, \tag{47}$$

where $V = (\mu_L - \mu_R)/e$ is the voltage drop. The average transmission coefficient is defined as

$$\langle T(E) \rangle = \int_0^{\pi/2} \mathrm{d}\theta\; T(E,\theta)\, \cos\theta. \tag{48}$$

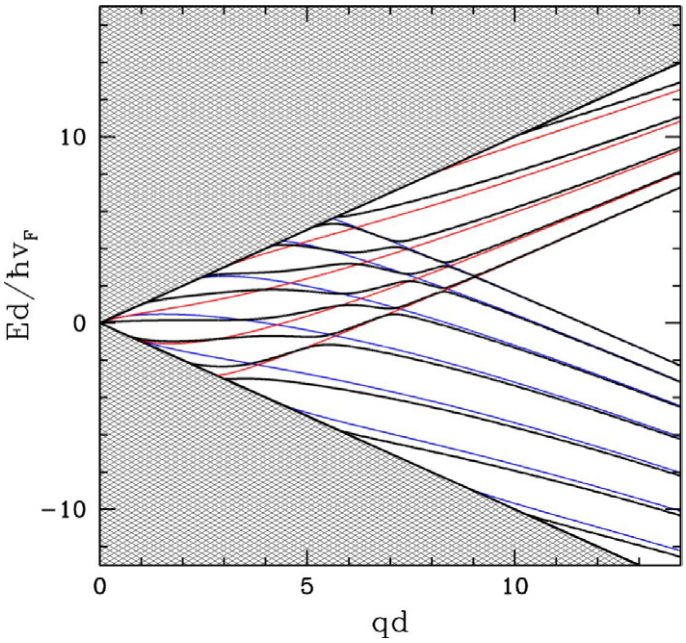

Figure 10. Subband structure and bulk Dirac cones for the p–n junction with $d_1 = d_2 = d$ and $V_1 = 12\hbar v_F/d$, $V_2 = -7\hbar v_F/d$, shown in black. Superimposed in blue and red are the subband structures for the individual V_1 and V_2 barriers, respectively.

The carrier density at zero temperature is $n = gk_F^2/4\pi$, so the Fermi energy is $E_F = \hbar v_F k_F = \hbar v_F\sqrt{4\pi n/g}$. Thus,

$$I(V) = \frac{e^2}{\pi h}\,\langle T(E_F)\rangle\,(4\pi g n)^{1/2}\,L_y\,V. \tag{49}$$

Defining the effective channel number,

$$N_c = \frac{g}{\pi}\,k_F L_y = (4gn/\pi)^{1/2}\,L_y, \tag{50}$$

the two-terminal Landauer conductance becomes

$$G = \frac{I}{V} = N_c \times \frac{e^2}{h}\,\langle T(E_F)\rangle. \tag{51}$$

Expressed in a convenient set of units, the resistance is

$$\begin{aligned} R = G^{-1} &= \frac{h}{N_c\,e^2} \times \langle T(E_F)\rangle^{-1} \\ &= 0.114\,\mathrm{k\Omega}\cdot\langle T(E_F)\rangle^{-1}\cdot\bar{n}^{-1/2}\cdot\bar{L}_y^{-1}, \end{aligned} \tag{52}$$

where $\bar{n}$ is the dimensionless carrier density (in the leads) in units of $10^{12}\,\mathrm{cm}^{-2}$ and $\bar{L}_y$ is the length of the barrier region in units of microns.

For a single trench of width d_1 and carrier density n_1 embedded between graphene leads of carrier density n_0, we have $\mathcal{M} = M_0^{-1}\,Q_1\,M_0$, where $Q_j \equiv M_j\,K_j M_j^{-1}$ and

$$\mathrm{Re}\,\mathcal{M}_{11} = \cosh\omega_1, \tag{53}$$

$$\mathrm{Im}\,\mathcal{M}_{11} = \sigma_0\,\sigma_1\sinh\omega_1\tan\varphi_1\sec\theta_0 - \sinh\omega_1\sec\varphi_1\tan\theta_0. \tag{54}$$

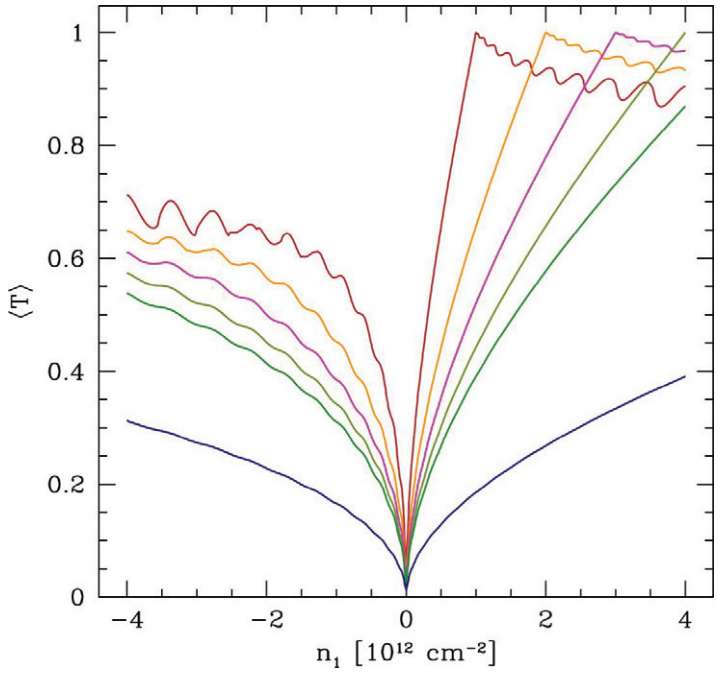

Figure 11. Average transmission coefficient across a single trench of width $d_1 = 100\,\text{nm}$ as a function of density n_1 (in units of $10^{12}\,\text{cm}^{-2}$). From top to bottom: $n_0 = 1, 2, 3, 4, 5$ and 20 ($\times 10^{12}\,\text{cm}^{-2}$). Negative densities correspond to a p-type (hole-doped) trench.

Here we have assumed that $k_1 < q$, so the trench contains evanescent solutions, but by a simple analytic continuation our result also holds for the $k_1 > q$ case.

For an embedded junction consisting of two consecutive slabs (n_1, d_1) and (n_2, d_2), the total transfer matrix is $\mathcal{M} = M_0^{-1}\, Q_1\, Q_2\, M_0$, resulting in

$$\text{Re}\,\mathcal{M}_{11} = \cosh\omega_1 \cosh\omega_2 + \sinh\omega_1 \sinh\omega_2\,(\sec\varphi_1 \sec\varphi_2 - \sigma_1\,\sigma_2\,\tan\varphi_1 \tan\varphi_2), \tag{55}$$

$$\begin{aligned}\text{Im}\,\mathcal{M}_{11} = {} & \sigma_0\,\sigma_1\,\sec\theta_0 \sinh\omega_1 \tan\varphi_1 \cosh\omega_2 + \sigma_0\,\sigma_2\,\sec\theta_0 \cosh\omega_1 \sinh\omega_2 \tan\varphi_2 \\ & - \tan\theta_0\,(\cosh\omega_1 \sinh\omega_2 \sec\varphi_2 + \sec\varphi_1 \sec\varphi_1 \cosh\omega_2).\end{aligned} \tag{56}$$

In figure 11, we plot the average transmission coefficient $\langle T(E_\text{F})\rangle$ as a function of the density n_1 for a single trench with $d_1 = 100\,\text{nm}$, for several different values of the lead density n_0. There are three features worth noting. Firstly, there is a non-zero transmission even when $n_1 = 0$, due to the presence of evanescent solutions within the trench [30]. Secondly, there is (obviously) perfect transmission when $n_1 = n_0$. Thirdly, the transmission falls off rapidly as $n_1 \to 0$, and is smooth for $0 < n_1 < n_0$, which is a regime where the carriers in both regions are of the same sign, yet total internal reflection can occur at the interface, with the critical angle given by $\sin\theta_0^\text{c} = |n_1/n_0|^{1/2}$. Finally, when $n_1 > n_0$ or when the carriers in the leads and the trench are of opposite sign, one observes quantum oscillations in the transmission, due to constructive and destructive interference effects from scattering at the walls of the trench.

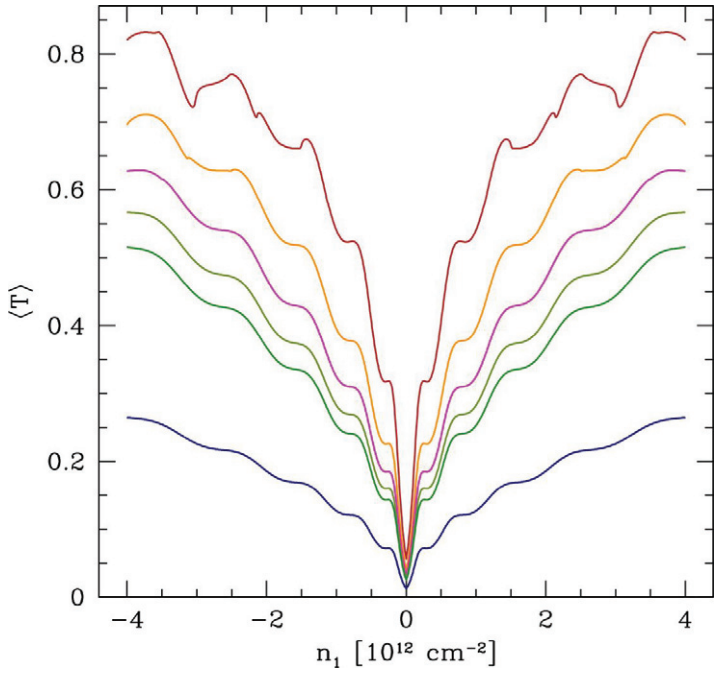

Figure 12. Average transmission coefficient across an embedded p–n junction with $d_1 = d_2 = 50$ nm as a function of density $n_1 = -n_2$ (in units of 10^{12} cm^{-2}). From top to bottom: $n_0 = 1, 2, 3, 4, 5$ and 20 ($\times 10^{12}$ cm^{-2}).

It is interesting to compare figure 11 with the results in [11], which reports the measured conductance through an electrostatically defined trench potential in a wide graphene ribbon as a function of the gate voltage defining the trench. As in our results, the experiments indicate a rapidly falling conductance when n_1 has the same sign as n_0, as n_1 approaches zero, and after passing through zero one observes oscillations due to quantum interference. A prominent difference is the absence in the experimental results of a rising background around which these oscillations occur. In our model, this appears because the density of states in the trench increases as $|n_1|$ increases. It is likely that the difference between our theoretical results and those observed in [11] are due to the relatively smooth potential induced by the remote gates in the experiment. In particular, this can yield relatively large 'depletion' regions between the trench and the graphene leads, which may dominate the resistance of the device and overwhelm the increase in conductance related to the trench density of states. In principle, one could model the device as a series of piecewise constant potentials and use the transfer matrix method we have developed to obtain a more quantitatively accurate model.

In figure 12, we plot $\langle T(E_F)\rangle$ as a function of n_1 for an embedded p–n junction with $d_1 = d_2 = 50$ nm and $n_2 = -n_1$. For such a symmetric junction, the average transmission is symmetric under $n_1 \to -n_1$. The step-like features present in the transmission here represent scattering effects due to the localized solutions and the avoided crossings in their dispersions, as discussed in the previous section. Thus, the bound states support an (in principle) measurable signature in conductance through the system.

6. Summary

In this paper, we have studied the spectra of and transport properties through graphene in the presence of several piecewise constant potentials. We demonstrated that these may be

investigated in a straightforward manner using a transfer matrix approach [27, 28]. For the case of superlattice potentials, we demonstrated that exact solutions of the Dirac equation generically contain Dirac points centered at zero energy for particle–hole symmetric potentials [25, 26], and that these are special cases of Dirac points that appear throughout in the band structure of superlattice potentials. We also considered the cases of a single trench and an embedded p–n junction in neutral graphene, both of which may support confined states at large enough values of k_y, the momentum along the translationally invariant direction. An analysis of conductance through these structures shows quantum interference effects, which may be interpreted as signatures of these bound states, in principle allowing these unique features of graphene nanostructures to be seen experimentally.

Note added: While this manuscript was in the final stages of preparation, a manuscript by Barbier, Vasilopoulos and Peeters appeared [27] that also considers the effect of a superlattice on monolayer graphene and the emergence of additional Dirac points. We are grateful to F M Peeters for subsequently alerting us to the substantial previous work that he and his collaborators have contributed to the subject of Dirac subband spectra and transport in the presence of 1D potentials [21]–[23]. We are also grateful to Y P Bliokh for drawing our attention to [24], which also addresses subband formation in the presence of a superlattice structure.

Acknowledgments

DPA thanks M Fogler for helpful discussions. Funding was provided by the MEC-Spain via grant number FIS2009-08744 (LB) and by the NSF through grant numbers DMR-0704033 (HAF) and EEC-0646547 (EAK). DPA, LB, HAF and KZ acknowledge the hospitality of the Benasque Physics Center (Spain), where this work was initiated.

Appendix

We define $Q = MKM^{-1}$ for a given slab. Within a propagating slab, we have

$$Q = \begin{pmatrix} \cos\chi + \sin\chi\,\tan\theta & \mathrm{i}\sigma\,\sin\chi\,\sec\theta \\ i\sigma\,\sin\chi\,\sec\theta & \cos\chi - \sin\chi\,\tan\theta \end{pmatrix}, \tag{A.1}$$

with $\chi = kd\cos\theta$, while for a non-propagating slab, we have

$$Q = \begin{pmatrix} \cosh\omega + \sinh\omega\,\sec\varphi & \mathrm{i}\sigma\,\sinh\omega\,\tan\varphi \\ \mathrm{i}\sigma\,\sinh\omega\,\tan\varphi & \cosh\omega - \sinh\omega\,\sec\varphi \end{pmatrix}, \tag{A.2}$$

with $\omega = kd\,\cot\varphi$. These expressions are useful in constructing the transfer matrix for a series of slabs, which is given in equation (31).

References

[1] Geim A K and Novoselov K S 2007 *Nat. Mater.* **6** 183
[2] Neto A H C, Guinea F, Peres N M R, Novoselov K S and Geim A K 2009 *Rev. Mod. Phys.* **81** 109
[3] Molitor F, Huefner M, Jacobsen A, Pioda A, Stampfer C, Ensslin K and Ihn T 2009 arXiv:0904.1364
[4] Luo T, Iyengar A, Fertig H and Brey L 2009 *Phys. Rev.* B **80** 165310
[5] Abergel D S L, Apalkov V M and Chakraborty T 2008 arXiv:0806.2854
[6] Bahamon D A, Pereira A L C and Schulz P A 2008 arXiv:0812.2001

[7] Potas P, Guclu A D and Hawrylak P 2009 arXiv:0908.3693
[8] Wurm J, Wimmer M, Baranger H and Richter K 2010 *Semicond. Sci. Technol.* **25** 034003
[9] Novikov D S 2005 *Phys. Rev.* B **72** 235428
[10] Stander N, Huard B and Goldhaber-Gordon D 2009 *Phys. Rev. Lett.* **102** 026807
[11] Young A and Kim P 2009 *Nat. Phys.* **5** 222
[12] Cheianov V V, Fal'ko V and Altshuler B 2007 *Science* **315** 1252
[13] Zhang L M and Fogler M M 2008 *Phys. Rev. Lett.* **100** 116804
[14] Beenakker C 2008 *Rev. Mod. Phys.* **80** 1337
[15] Velasco J, Liu G, Bao W and Lau C N 2009 arXiv:0907.3366
[16] Pereira J M, Mlinar V, Peeters F M and Vasilopoulos P 2006 *Phys. Rev.* B **74** 045424
[17] Pletikosic I, Kralj M, Pervan P, Brako R, Coraux J, N'Diaye A, Busse C and Michely T 2009 *Phys. Rev. Lett.* **102** 056808
[18] Tiwari R and Stroud D 2009 arXiv:0901.4780
[19] Esmailpour A, Abedpour N, Asgari R and Tabar M R R 2008 arXiv:0809.4578
[20] Park C, Son Y-W, Yang L, Cohen M L and Louie S G 2008 *Nano Lett.* **8** 2920
[21] Pereira J M Jr, Peeters F M and Vasilopoulos P 2007 *Appl. Phys. Lett.* **90** 132122
[22] Barbier M, Peeters F M, Vasilopoulos P and Pereira J M Jr 2008 *Phys. Rev.* B **77** 115446
[23] Barbier M, Peeters F M and Vasilopoulos P 2009 *Phys. Rev.* B **80** 205415
[24] Bliokh Y P, Freilikher V, Savel'ev S and Nori F 2009 *Phys. Rev.* B **79** 075123
[25] Brey L and Fertig H 2009 *Phys. Rev. Lett.* **103** 046809
[26] Park C, Son Y-W, Yang L, Cohen M L and Louie S G 2009 *Phys. Rev. Lett.* **103** 046808
[27] Barbier M, Vasilopoulos P and Peeters F M 2010 arXiv:1002.1442
[28] Yampolksii Y, Savelev S and Nori N 2008 *New J. Phys.* **10** 053024
[29] Arnold V I 1973 *Ordinary Differential Equations* (Cambridge, MA: MIT Press) p 28
[30] Tworzydlo J, Trauzettel B, Titov M, Rycerz A and Beenakker C W J 2006 *Phys. Rev. Lett.* **96** 246802
[31] Wurm J, Rycerz A, Adagideli I, Wimmer M, Richter K and Baranger H U 2009 *Phys. Rev. Lett.* **102** 056806